

X-ray Standing Wave Imaging

M. J. BEDZYK,^{1,2} P. FENTER,² Z. ZHANG,^{1,2} L. CHENG,²
J. S. OKASINSKI,¹ AND N. C. STURCHIO^{2,3}

¹Institute of Environmental Catalysis, Northwestern University, Evanston, IL 60208, USA

²Argonne National Laboratory, Argonne, IL 60439, USA

³University of Illinois at Chicago, Chicago, IL 60607, USA

Introduction

The continuing need to understand the structure-property relationships in various materials systems (electronic, geochemical, biological, etc.) strongly motivates the development of new and powerful experimental techniques that seek to *directly* observe structures (e.g., crystals, surfaces) at the atomic scale. Crystallographic approaches such as X-ray diffraction are the workhorses of structure determination, but the loss of phase information in scattering data can be a significant impediment. Holographic techniques have been shown to provide model-independent images of atomic structures [1–3], but have limitations in the range of systems that can be studied.

It has long been recognized that the X-ray standing wave (XSW) technique [4, 5], unlike traditional crystallographic techniques, is directly sensitive not only to the amplitude of the structure factor but also its phase [6]. This measured phase information provides numerous benefits concerning the ability to determine the precise locations of atoms, both within a crystal and at (and above) a crystal surface, as described throughout this issue. Measurements of characteristic X-ray induced emissions (e.g., X-ray fluorescence), as a function of incident angle at the $H = hkl$ Bragg reflection (with Bragg plane spacing d_H), reveal the H th Fourier coefficients F_H of the element-specific, normalized density $\rho(\mathbf{r})$ (including both its amplitude f_H and phase P_H , also referred to as the coherent fraction and position, respectively) [7–10]. That is,

$$F_H = \int_{uc} \rho(\mathbf{r}) \exp(2\pi i \mathbf{H} \cdot \mathbf{r}) d\mathbf{r} = f_H \exp(2\pi i P_H) \quad (1)$$

In standard crystallographic terminology, F_H is the normalized *geometrical* structure factor for an element-specific sublattice.

The typical XSW analysis treatment uses the measured values of f_H and P_H to derive structural parameters by comparison to a simple model. This model-dependent approach is necessarily limited, especially when applied to non-trivial elemental distributions whose nature and complexity may not be initially apparent. As recently demonstrated [11–13], a more general approach for determining the 3D atomic density map, $\rho(\mathbf{r})$, is to directly sum the XSW-measured Fourier components ρ_H as follows:

$$\begin{aligned} \rho(\mathbf{r}) &= \sum_H \rho_H(\mathbf{r}) = \sum_H F_H \exp(-2\pi i \mathbf{H} \cdot \mathbf{r}) \\ &= 1 + 2 \sum_{\substack{H \neq -H \\ H \neq 0}} f_H \cos[2\pi(P_H - \mathbf{H} \cdot \mathbf{r})] \end{aligned} \quad (2)$$

The above simplification to a summation of cosine terms over half of reciprocal space uses a general symmetry relationship analogous to Friedel's law that makes $f_{\bar{H}} = f_H$ and $P_{\bar{H}} = -P_H$. Note also that using a *normalized* distribution makes $f_0 = 1$. This model-independent approach is simple, straightforward, and robust as long as a sufficiently complete set of F_H coefficients are measured. Since this set is restricted to allowed hkl reflections from the bulk crystal, the resulting density map for a fluorescence selected atom will be a projection of the true extended distribution into the primitive unit cell of the bulk single crystal.

The schematic in Figure 1 illustrates a 1D Fourier synthesis that uses model-calculated amplitudes and phases for the atomic planes in the diamond cubic structure along the $\mathbf{H} = hhh$ direction. The amplitude and phase of successive Fourier coefficients vary with \mathbf{H} due to the two layers at $z = \pm 1/8$ within the 1D unit cell, which has a lattice constant equal to d_{111} . The density profile, determined by summing the 000 to 888 individual Fourier components as described in Eq. 2, directly reveals the presence of two layers within the unit cell that are fully resolved. This simple simulation illustrates the central characteristics of this approach; namely, that for a Fourier summation in the \mathbf{H} direction that terminates at the H_{\max} term: (1) oscillations due to termination error appear in the density profile with a period of $d_{H\max}$; and (2) the resolution in the \mathbf{H} direction is equivalent to $d_{H\max}/2$. Thus in this particular model calculation, the resolution is $\sim d_{111}/16$. As the experimental resolution approaches the actual width of the intrinsic distribution, the termination oscillations are dampened more clearly revealing the actual distribution. This is illustrated in Figure 1 where $\rho(z)$ is recalculated with two Gaussian functions ($\sigma = 0.03 \cdot d_{111}$) that roughly simulate the time-averaged distribution corresponding to room temperature thermal vibrations.

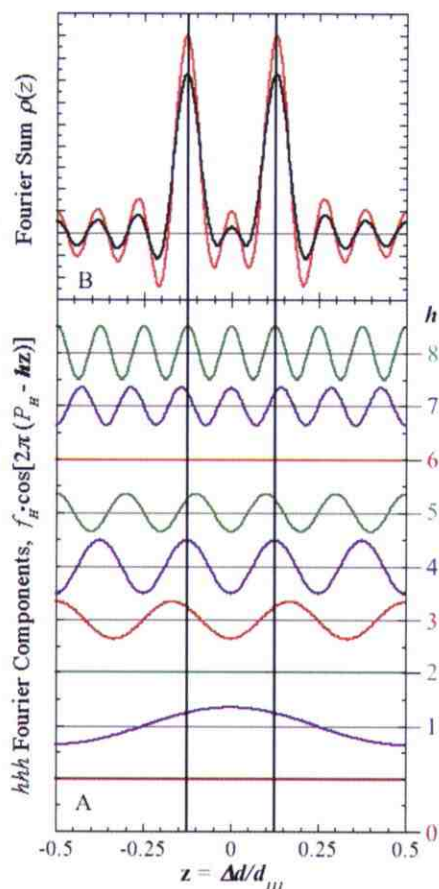


Figure 1: Fourier synthesis of a 1D diamond lattice density profile $\rho(z) = 1/2[\delta(z - 1/8) + \delta(z + 1/8)]$ along the [111] direction using calculated Fourier coefficient amplitudes (f_{hhh}) and phases (P_{hhh}) with $h = 0, 1, 2, \dots, 8$. For this case $f_{hhh} = |\cos(\pi h/4)|$, making $f_{000} = f_{444} = f_{888} = 1$, $f_{111} = f_{333} = f_{555} = f_{777} = 1/2$, and $f_{222} = f_{666} = 0$. The origin for the normalized coordinate z is placed at the center of the bilayer making $P_{111} = P_{777} = P_{888} = 0$, and $P_{333} = P_{444} = P_{555} = 1/2$. (A) Each separate Fourier component, $1/2(\rho_F + \rho_H) = f_{hhh} \cos(2\pi(P_{hhh} - hz))$, is vertically offset with horizontal gray lines indicating the zero-level. (B) The Eq. 2 summed profile in red shows clear peaks corresponding to the ideal atom positions at $z = \pm 1/8$ (two vertical lines). Also shown is a second simulation where each delta-function is replaced by a $\sigma = 0.03 \cdot d_{111}$ Gaussian to simulate finite vibrational amplitude. In which case, $f_{hhh} = |\cos(\pi h/4)| \exp(-2(\pi h \sigma/d_{111})^2)$. Ignoring anomalous dispersion effects, the diamond-cubic structure factor is in-phase with the geometrical structure factor and hence the curves in (A) also represent the phase and period of the XSW at the high-angle side of the hhh Bragg peak for $\Delta f'' = 0$. (Anomalous dispersion phase shifts the structure factor and the XSW[6].)

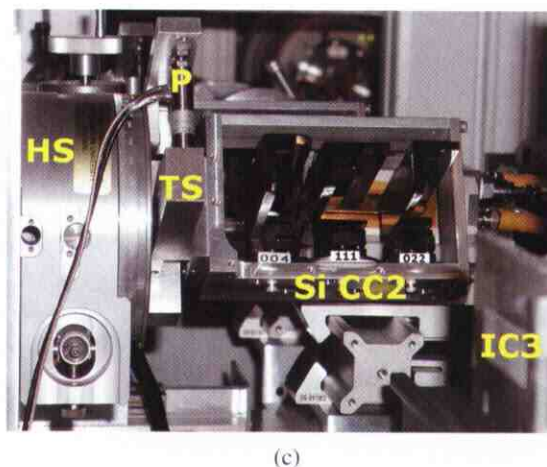
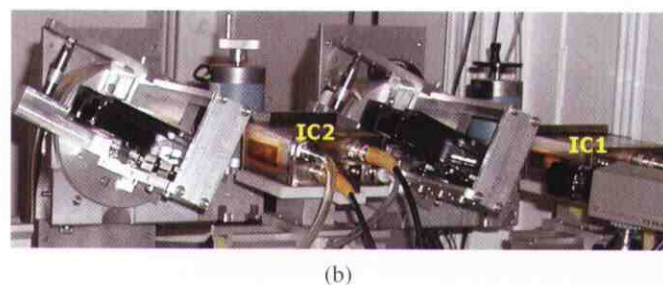
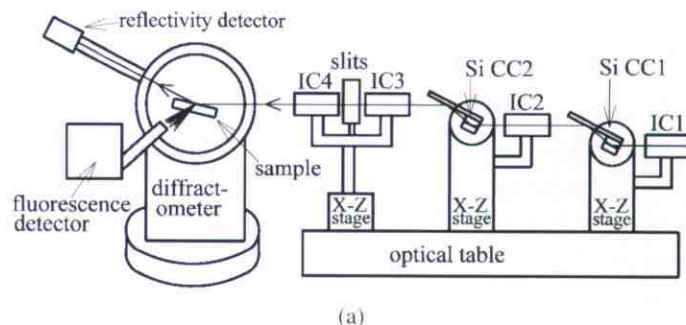


Figure 2: Experimental system. (a) Side view schematic of the experimental components: four ion chambers (IC) monitor the X-ray flux after the beam is conditioned by the post-monochromator components. Two pairs of Si channel-cut monochromator (Si CC) reduce the energy bandpass and angular divergence of the X-rays incident on the sample; (b) Side view image of the post-monochromator components tuned to the Si(111) reflection at 7.0 keV; (c) Image showing upstream view of channel-cut monochromator mounted on a torsion-bearing stage (TS) attached to a Huber 410 rotary stage (HS). A piezo actuator (P) uses feedback from the ion chambers to maintain a fixed detuning value for the Si channel-cut monochromators.

An experimental end-station used for these studies is shown as a photograph and schematic in Figure 2. The end-station uses two non-dispersive double-bounce silicon post-monochromators with a d-spacing typically chosen to closely match that of the selected Bragg planes of the sample. Each of the two rotational stages is equipped with a set of remotely selectable Si (hhh), (hh0), and (00h) channel-cut crystals. The incident beam channel-cut monochromators are used, either individually or in tandem, to tune the X-ray beam dispersion characteristics and optimize the measurement to best match the various Bragg reflections for the sample. More specifically, it is important to optimize the observed fluorescence modulation to improve the experimental sensitivity for measuring a particular Fourier coefficient. This flexibility of changing the λ vs. θ emittance function of the postmonochromator for each reflection of the sample is important because the strength/weakness of a substrate Bragg reflection is, in general, unrelated to the importance of that Fourier component to the elemental density profile to be measured. Consequently, all Fourier components in a particular direction up to H_{\max} should be measured to obtain an image.

Applications to bulk, vacuum-solid and liquid-solid interfaces

The first demonstration of this XSW imaging approach as a structural tool concerned the measurement of one-dimensional impurity site distributions within the muscovite ($2M_1$) crystal lattice [11]. Muscovite is a form of mica that has an end member formula of $K_2Al_4(Si_3Al)_2O_{20}(OH)_4$. The unit cell is depicted in the top portion of Figure 3. XSW measurements were made for the (00L) set of Bragg reflections for $L = 2, 4, 6, \dots, 16$.

The use of an energy dispersive solid-state detector allowed the simultaneous measurement of X-ray fluorescence (XRF) from the major lattice heavy-elements (K, Al, Si) and several lattice impurities (Fe, Mg, Ti, Ba). Comparison of measured and model-calculated profiles for major elements (Figure 3) confirmed the internal consistency of this approach by direct comparison of simulated and Fourier-synthesized profiles. Model-independent elemental impurity profiles (Figure 3) confirmed the expected site distributions for these cations. This analysis does not impose any assumptions on the derived impurity structures since it relies only on information about the host crystal structure and the incident X-ray beam properties. From the XSW atom distribution profiles and the accompanying XRF elemental composition analysis the cation portion of the muscovite formula (for this particular specimen) was reconstructed as:

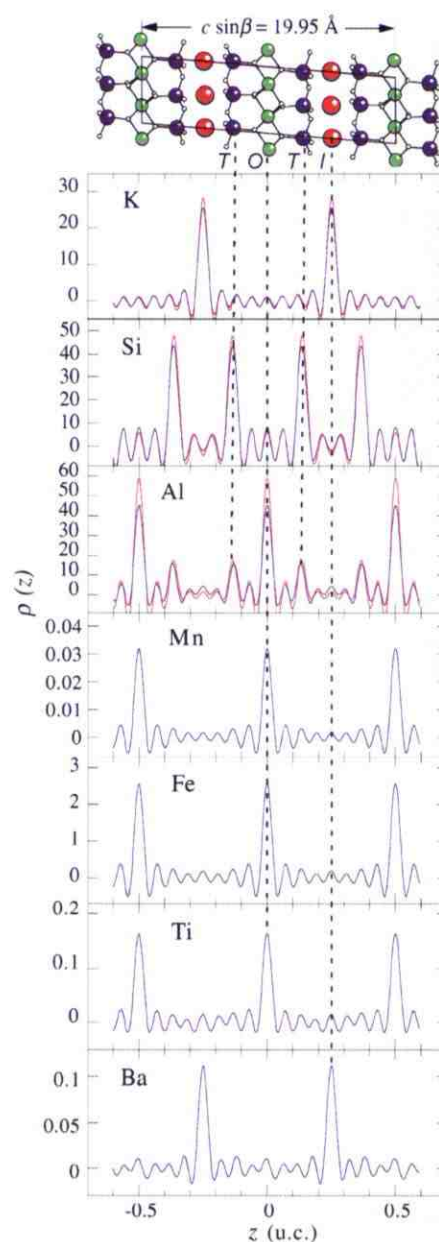


Figure 3: Perspective view of the muscovite lattice with derived 1D elemental profiles in the muscovite (001) unit cell derived from measurements of the (00L) reflections with $L = 2, 4, \dots, 16$. Derived and simulated major element distributions (K, Al, Si) agree demonstrating the internal consistency of the approach, showing K in the interlayer site (I), Si in the tetrahedral site (T), and Al in both tetrahedral and octahedral sites (O). The model-independent impurity distributions show Mn, Fe, Ti in the tetrahedral site, and Ba in the interlayer site, as expected.

interlayer site	octahedral site	tetrahedral site
$(K_{1.87}Ba_{0.008})$	$(Al_{3.50}Mn_{0.002}Fe_{0.18}Ti_{0.013})$	$(Si_{3.17}Al_{1.01})_2$

High Precision Slits

SL 100 Series



- Motion Repeatability: 0.00004 in (1 micron)
- Motion Resolution: 0.000016 in (0.4 micron)
- Maximum slits opening 1 in (25 mm)
- With all control electronics onboard
- Finger control with LED indicators
- Rotary Encoders
- Crossed roller bearing technology
- Zero backlash
- Vacuum compatible 10^{-4} Torr (NW40 mount)
- Sharp polished edge paddles, 0.5×10^{-6} in (0.013 microns - Mirror finish), with 2 degree chamfered section
- Blades can go "past closed" without crunching (Overlapping/Zero beam)
- Blade material: Tantalum or Tungsten

SL 200 Series



- Motion Repeatability: 0.00004 in (1 micron)
- Motion Resolution: 0.000016 in (0.4 micron)
- Maximum slits opening 0.5 in (12.5 mm)
- Crossed roller bearing technology
- Zero backlash
- Vacuum compatible 10^{-4} Torr (NW40 mount)
- Sharp polished edge paddles, 0.5×10^{-6} in (0.013 microns - Mirror finish), with 2 degree chamfered section
- Blades can go "past closed" without crunching (Overlapping/Zero beam)
- Blade material: Tantalum or Tungsten

SL 300 Series



- Ultra High Vacuum (UHV) 5×10^{-10} Torr
- Motion Repeatability: 0.00004 in (1 micron)
- Motion Resolution: 0.000016 in (0.4 micron)
- Maximum slits opening (4 Sizes)
- Available in 4.5, 6, 8, 10 inch flanges
- Crossed roller bearing technology
- Zero backlash
- Sharp polished edge paddles, 0.5×10^{-6} in (0.013 microns - Mirror finish), with 2 degree chamfered section
- Blades can go "past closed" without crunching (Overlapping/Zero beam)
- Blade material: Tantalum or Tungsten

For more information contact:

Advanced Design Consulting, Inc.

Corporate Headquarters

126 Ridge Road, P.O. Box 187, Lansing, NY 14882

Tel (607) 533-3531 • Fax (607) 533-3618

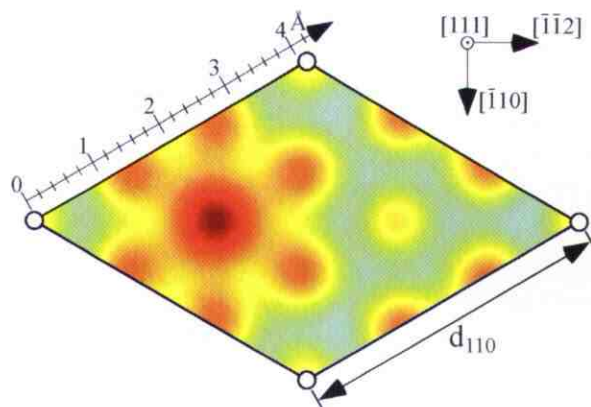
Web: www.adc9001.com • E-mail: adc@adc9001.com



Notice how the peaks in the 1D density distributions have a FWHM $\sim 0.8 \text{ \AA}$, which is close to the expected resolution of $1/2 d_{0016} = 0.62 \text{ \AA}$.

After this initial case for 1D imaging of bulk impurity distributions, 3D images were produced for a series of surface adsorbate problems [12, 13]. One of the UHV surfaces studied was the $1/3 \text{ ML Sn/Ge}(111)$ surface that exhibits a $(\sqrt{3} \times \sqrt{3})R30^\circ$ to (3×3) reversible phase transition at $T_C \sim 210 \text{ K}$ [14]. The XSW analysis confirmed earlier STM and

Top view along $[111]$ at height of 2.0 \AA



Side view along $\bar{1}10$ and at the diagonal

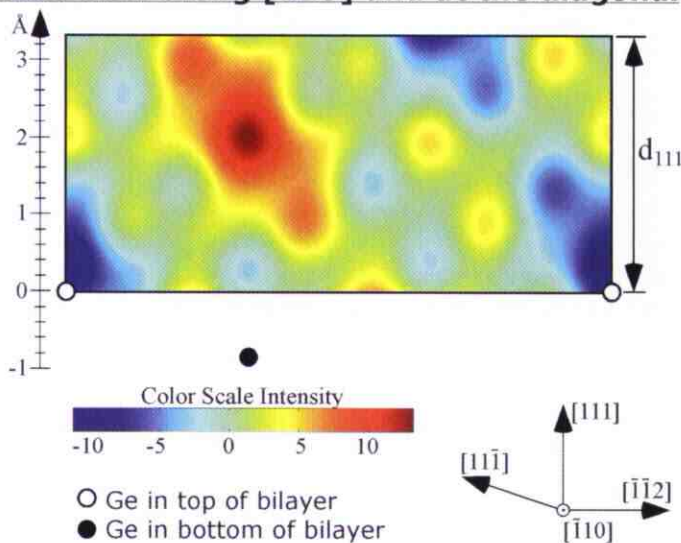


Figure 4: XSW direct space atomic density maps for the $1/3 \text{ ML Sn/Ge}(111)$ surface at room temperature. The XSW measurement projects the extended structure into the primitive unit cell of the Ge bulk crystal. The top view corresponds to the (1×1) 2D unit cell and confirms that Sn occupied the T_4 -adsorption site. Black circles are added to the images to represent the bulk-like Ge atoms in the top two layers.

SXRD [15] results that placed the Sn atoms in both phases at T₄-adsorption sites. This can be seen in the XSW image of the RT Sn distribution shown in Figure 4. This image was generated by the Eq. 2 summation over the XSW measured (111), (333), (11-1), and (33-3) cosine terms, plus additional 3-fold symmetry related terms. This same XSW data is then given a conventional XSW analysis with a model that laterally constrains the Sn to only appear at T₄-sites, as derived from the model-independent images. This analysis reveals that one-third of the Sn are displaced upward by 0.45 Å. This “2-down and 1-up” Sn configuration was found to be “frozen-in” below TC consistent with the 3 × 3 long-range ordered phase seen by STM, SXRD and LEED. Interestingly, the XSW measured local time-averaged Sn distribution was unchanged above TC with “2-down and 1-up,” even though the STM image shows all Sn at the same height and LEED and SXRD exhibits the higher symmetry ($\sqrt{3} \times \sqrt{3}$)R30° phase. This supports a dynamical fluctuation model [16] and an order-disorder phase transition for this 2D system.

Returning our attention to the details of the model-independent XSW image, notice that the three separate Sn atoms at two different heights in the extended 2D superlattice are merged together at the same T₄ site in the XSW image. This is due to the projection of $\rho(r)$ into the Ge primitive unit cell as discussed above. Although the image cannot resolve the two different heights (i.e., the (444) and (555) coefficients

would need to be included), a bottom-heavy oblong distribution can be extracted from the image.

The first application of this approach to the liquid-solid interface revealed the 3D ion site distributions of Sr²⁺, Zn²⁺, and Y³⁺ at the rutile (α -TiO₂)-water interface [13]. Full 3D model-independent images of the elemental distributions (shown as a color map in Figure 5) are obtained with Eq. 2, using the (110), (200), (101), (111) and (211) reflections, making use of the rutile (110) surface symmetry for symmetry-equivalent reflections. Slices through the derived 3D distributions at the plane of maximum density reveal that Sr²⁺ and Y³⁺ are adsorbed at a “tetradentate” site between two terminal oxygen sites (TO) and two bridging oxygen sites (BO). In contrast, Zn²⁺ appears to be adsorbed at two distinct sites (each at a different height), primarily above a single BO and to a lesser extent in a bidentate adsorption site between TOs. The ability to resolve the two distinct Zn²⁺ adsorption sites with no more difficulty than determining the substrate atom locations or the simpler distributions for Sr²⁺ and Y³⁺ illustrates the power of this model-independent analysis of XSW data, and is especially important for understanding complex ion distributions. In cases such as this, where only a limited number of Bragg reflections were measured, care must be taken to avoid identifying peaks associated with Fourier series termination as actual atom sites. Consequently these model-independent images are best used as a starting point for subsequent quantitative analysis of the

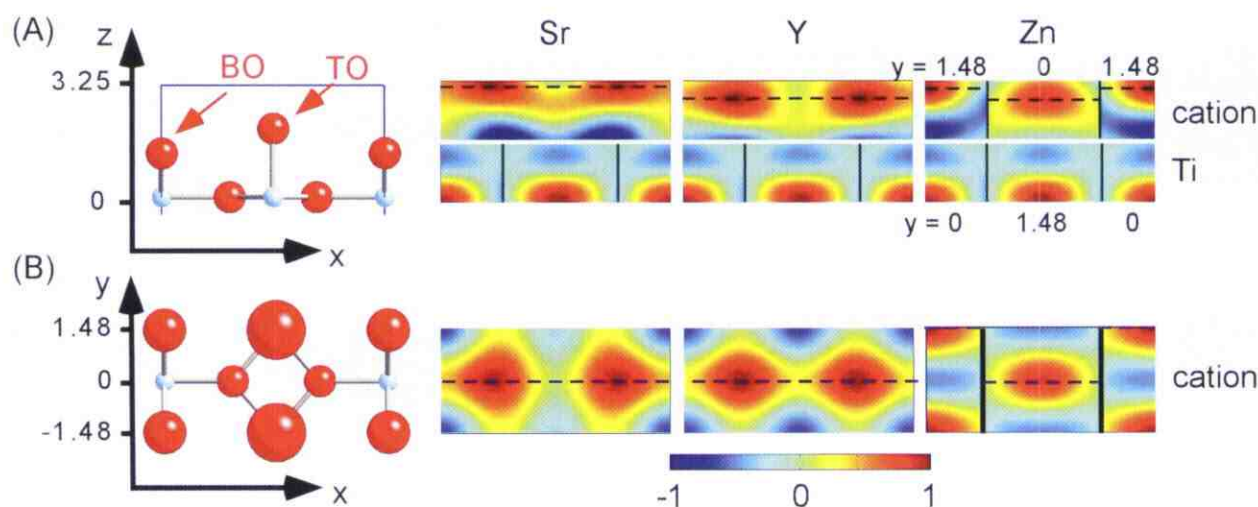


Figure 5: (A) Perspective side view of the rutile (110) surface with the measured vertical distributions of Ti (from the TiO₂ substrate), and cations Sr²⁺, Y³⁺ and Zn²⁺ adsorbed to rutile shown as a cuts through the plane of maximum density. (B) Perspective top view of the rutile (110) surface along with cuts through the lateral ion distributions. Dashed lines in the vertical distributions indicate the height of the corresponding lateral distributions (and vice versa). Differences in the ion heights and their lateral locations can be immediately observed. Intensity scale bar for ion distributions is shown as inset at bottom. Axes adjacent to perspective views correspond to: x along [1-10], y along [001] and z along [110]. Perspective views are shown with oxygen in red, titanium in blue, with bridging oxygen (BO) and terminal oxygen (TO) rows along the [001] direction, with heights of 1.265 Å and 1.983 Å above the Ti-O plane, respectively.

precise adsorbate locations by comparison of measured and calculated f_H and P_H . For example, such an analysis yields the relative coverage of Zn^{2+} in the two distinct adsorption sites and reveals that both Zn^{2+} species are displaced from their nominal high-symmetry adsorption sites [17].

Discussion and future prospects

It would be of interest to extend the 3D bulk crystal impurity example of this XSW imaging technique toward solving structural problems within lattices of higher complexity, including heavy atom imaging in protein crystals. This XSW imaging approach could also be extended to larger-scale distributions that extend beyond the dimensions of typical substrate crystallographic unit cells. This could in principle be accomplished with other variations of the XSW technique that employ standing waves with longer periods (e.g., through total external reflection or reflection from layered synthetic multilayers [18]), thereby allowing characterization of structures that extend $>100 \text{ \AA}$ from the surface. Therefore, a more complete and direct determination of elemental 1D distribution profiles at the liquid-solid interface (or within self-assembled multilayers) can also be achieved for various phenomena with distributions that have largely defied direct characterization, ranging from the diffuse layer distributions in the electric double-layer to biomolecular adsorption at membranes. ■

Acknowledgement

The authors thank the U.S. Department of Energy, Office of Basic Energy Sciences, Division of Chemical Sciences, Geosciences, and Biosciences, and the National Science Foundation MRSEC program for support of this research. Work was performed at the Advanced Photon Source (beamlines 12-ID-D, BESSRC-CAT and 5ID-C, DND-CAT) and the National Synchrotron Light Source (beamline X15A), which are supported by the U. S. Department of Energy. DND-CAT is partially supported by the State of Illinois under IBHE-HECA.

References

1. S. Omori, Y. Nihei, E. Rotenberg, J. D. Denlinger, S. Marchesini, S. D. Kevan, B. P. Tonner, M. A. Van Hove and C. S. Fadley, *Phys. Rev. Lett.* **88**, 055504 (1-4) (2002).
2. T. Gog, P. M. Len, G. Materlik, D. Bahr, C. S. Fadley and C. Sanchez-Hanke, *Phys. Rev. Lett.* **76**, 3132-3135 (1996).
3. M. Tegze and G. Faigel, *Nature* **380**, 49-51 (1996).
4. B. W. Batterman, *Phys. Rev. Lett.* **22**, 703-705 (1969).
5. J. A. Golovchenko, J. R. Patel, D. R. Kaplan, P. L. Cowan and M. J. Bedzyk, *Phys. Rev. Lett.* **49**, 560-563 (1982).
6. M. J. Bedzyk and G. Materlik, *Phys. Rev. B* **32**, 6456-6463 (1985).
7. N. Hertel, G. Materlik and J. Zegenhagen, *Zeitschrift Fur Physik B—Condensed Matter*, **58** 199-204 (1985).
8. M. J. Bedzyk and G. Materlik, *Phys. Rev. B* **31** 4110-4112 (1985).
9. J. Zegenhagen, *Surf. Sci. Rep.* **18**, 199-271 (1993), and references therein.
10. M. J. Bedzyk and L. Cheng, *Rev. Mineral. Geochem.* **49**, 221-266 (2002), and references therein.
11. L. Cheng, P. Fenter, M. J. Bedzyk and N. C. Sturchio, *Phys. Rev. Lett.*, **90**, 255503-1-4 (2003).
12. J. S. Okasinski, D. A. Walko, C.-Y. Kim and M. J. Bedzyk, *Phys. Rev. B* **69**, R041401-1-4 (2004).
13. Z. Zhang, P. Fenter, L. Cheng, N. C. Sturchio, M. J. Bedzyk, M. L. Machesky, and D. J. Wesolowski, *Surf. Sci. Lett.*, **554** (2-3) L95-L100 (2004). See Ref. [17] for details.
14. J. M. Carpinelli, H. H. Weitering, M. Bartkowiak, R. Stumpf, and E. W. Plummer, *Phys. Rev. Lett.* **81**, 2108-2111 (1997).
15. O. Bunk, J. H. Zeyson, G. Falkenberg, R. L. Johnson, M. Nielsen, M. M. Nielsen, and R. Feidenhans'l, *Phys. Rev. Lett.* **83**, 2226-2229 (1999).
16. J. Avila, A. Mascaraque, E. G. Michel, M. C. Asensio, G. LeLay, J. Ortega, R. Pérez, and F. Flores, *Phys. Rev. Lett.* **82**, 442-445 (1999).
17. Z. Zhang, P. Fenter, L. Cheng, N. C. Sturchio, M. J. Bedzyk, M. Predota, A. Bandura, J. Kubicki, S. N. Lvov, P. T. Cummings, A. A. Chialvo, M. K. Ridley, P. Bénézeth, L. Anovitz, D. A. Palmer, M. L. Machesky and D. J. Wesolowski, *Langmuir*, in press (2004).
18. M. J. Bedzyk, G. M. Bommarito, M. Caffrey and T. L. Penner, *Science* **248**, 52-56 (1990).

Copyright of Synchrotron Radiation News is the property of Taylor & Francis Ltd and its content may not be copied or emailed to multiple sites or posted to a listserv without the copyright holder's express written permission. However, users may print, download, or email articles for individual use.